Postprint of: Pierpaoli M., Ficek M., Jakóbczyk P., Karczewski P., Bogdanowicz R., Self-assembly of vertically orientated graphene nanostructures: Multivariate characterisation by Minkowski functionals and fractal geometry, Acta Materialia, Vol. 214 (2021), 116989, DOI: 10.1016/j.actamat.2021.116989

Self-assembly of vertically oriented graphene nanostructures: multivariate characterisation by Minkowski functionals and fractal geometry

Mattia Pierpaoli[a,*], Mateusz Ficek[a], Paweł Jakobczyk[a], Jakub Karczewski[a], Robert Bogdanowicz[a]

[a]*Gdańsk University of Technology, ul. Narutowicza 11/12, 80-233 Gdańsk, Poland*

Abstract

The enormous self-assembly potential that graphene and its derived layered materials offer for responding to the contemporary environmental challenges has made it one of the most investigated materials. Hence, tuning its extraordinary properties and understanding the effect at all scales is crucial to tailoring highly customised electrodes. Vertically oriented graphene nanostructures, also known as carbon nanowalls (CNWs), due to the large surface area and unique maze-like morphology, have attracted attention as a platform for advanced sensing applications. In this work, a holistic investigation approach has been developed to disrupt the synthesis-composition-structure-property paradigm and to dig out the hidden materials relationships. To achieve that, autonomous advanced image-analysis methods (Minkowski Functionals, Fractal Analysis) have been applied to SEM micrographs and successfully classified them. Morphological, electrical, and electrochemical characterisation has been performed for all of the samples. Multivariate data analysis has been employed to mine the relationships between the material features, specifically as it relates to the understanding of the intrinsic properties. As a result, this study is intended to both shed light on CNWs as a promising transparent hybrid electrochemical substrate for perfectly assembled electrochemical devices and to provide a new flexible method for nanomaterial design, characterisation and exploitation.

Keywords: CVD, carbon nanowalls, electrochemical device, relationship mining, principal component analysis

---

[*] Corresponding author.

Email addresses: mattia.pierpaoli@pg.edu.pl (Mattia Pierpaoli), matficek@pg.edu.pl (Mateusz Ficek), pawel.jakobczyk@pg.edu.pl (Paweł Jakobczyk), jakub.karczewski@pg.edu.pl (Jakub Karczewski), rbogdan@eti.pg.edu.pl (Robert Bogdanowicz)

1. Introduction

Four fundamentals are critical in materials science and engineering: processing, structure, properties, and performance. According to Olson [1], these primary elements constitute the intersection of a three-link chain model, in which the deductive cause-and-effect logic proceeds according to the written order, while the inductive goal-means relations follows backwards. Carbon nanowalls (CNWs) are three-dimensional nanostructures, composed of vertically aligned stacks of graphene sheets. The most commonly adopted production method is by plasma-enhanced chemical vapour deposition (PECVD) on a suitable substrate. The process of nucleation and growth is dependent on several technical parameters, such as plasma power, temperature, pressure, applied bias and the composition of the gas precursor mixture. For this reason, tuning the electrical characteristics of CNWs represents an opportunity to develop advanced nanoarchitectured interfaces for highly specific applications, such as electrochemical sensing [2,3], environmental [4] and energy storage applications [5]. However, the synthesis of CNWs remains barely controlled and insufficiently understood, despite two decades of scientific research. CNWs can also be used as transparent electrodes. Depending on the method of production, CNWs of different shapes and properties are obtained [6–8]. Chongyin Yang et al. demonstrated a novel PECVD method to grow uniform graphene walls at 900 °C directly on SiO_2 and other dielectric substrates without using any catalyst. The presented graphene walls with a well-connected 3D structure possess high hydrophobicity (contact angle: 141°), outstanding electronic conductivity (sheet resistance: 198 Ωsq^{-1}) and tunable transparency (91.9–38.0% at 550 nm) [9]. Feng et al. fabricated a high-performance hybrid photodetector consisting of vertically aligned Gr arrays and $FAPbI_3$ quantum dots. The as-fabricated device exhibits superior optoelectronic performance with a high detectivity of $\approx 5.64 \times 10^{15}$ cm $Hz^{1/2}$ W^{-1} and a high responsivity of $\approx 2.17\ 10^{7}$ AW^{-1} under 1550 nm irradiation, which can be ascribed to the synergistic effects of FAPbI3 quantum dots and vertically aligned Gr arrays on light absorption, vertical electric field, and electron transportation [10]. Ozkan Bayram presented vertically oriented (3D) graphene nanostructures produced by using the PECVD technique on substrates such as Glass/FTO at relatively low temperatures (400 °C). The optical transmittance of the received structures ranged from 50% to 95% (at 550 nm wavelength) and their electrical conductivity was also determined to be between 5.94 kΩ/sqr and 11.2 kΩ/sqr [11]. Qi et al. have successfully achieved a one-step fabrication approach for high-performance supercapacitors (capacitance up to 1052 μF/cm^2) using vertically oriented few-layer graphene grown in situ on Pt nanocups to form 3D VFG-nanocup hybrid structured electrodes [12]. The incorporation of heteroatoms within the carbon lattice has been extensively investigated; in particular, the difference between N-incorporation and substitution [13], as well as the effect of boron-doping [14,15] to the wall morphology.

Machine learning techniques have been demonstrated to be exceptional at handling the large volume of data produced by scientists in materials research in many fields, such as the prediction of new stable materials, forecasting materials' properties, and mining the structure-property relationship, speeding up both fundamental and applied research. While it is possible to choose among different statistical tools, the first step is to have available the most complete and consistent dataset. A challenge is to translate imaging, spectroscopic and physical datasets into useful information on a material's structure for optimal understanding and controlling the material's functionality [16]. A model based on fractal geometry has already been successfully applied to characterisation in materials science. A non-exhaustive list of relevant studies is reported in the supplementary materials. Zahn & Zösch correlated the fractal dimension of STM images of Cr- and Si- nitride coatings obtained by magnetron sputtering with the variation of the gas pressure [17]. Fractal Analysis (FA) has been used to describe the nanostructure morphology of different carbon nanomaterials, such as graphene [18], carbon nanotubes [19] and microcrystalline diamonds [20], showing its effect on the substrates' adsorption ability [21], electrochemical activity [22], composition and adhesion strength [23]. Similarly to FA, which has found large employment in theoretical and experimental studies as a tool to describe and characterise morphological, physical and chemical self-similarities in different nanostructures, the use of Minkowski functionals (Mfs) has been reported in a very few studies [18,24], however, without arguing the reason of application or discussing the implication. Multivariate statistical analysis techniques have been employed by Bonnet for the analysis of microscope images [25] and by Widjaja and Garland to treat collected sets of vibrational spectra to successfully reverse-engineer a multi-layer packaging material [26]. Among these, Principal Component Analysis (PCA) seeks to reduce the observation dimensionality, by minimising the loss of information. In other words, for a *sufficiently large* number of samples, characterised by N correlated variables, it is possible to derive a new set of N uncorrelated descriptors (expressed as a linear combination of the original variables). By selecting the new descriptors, which express the highest variance, it is possible to highlight which of the original variables is better related to a specific sample feature. For this reason, PCA is helpful in screening and assessing the relative impact of multiple parameters on sample properties [27]. Cluster analysis (CA) is a powerful tool for rapidly classifying multivariate data into subgroups, based on the provided dataset: it can help uncover the characteristics of the sample structure or patterns present. In this study, starting from the synthesis process and proceeding through monitoring the CVD process by optical emission spectroscopy (OES), by characterising the nanostructures and assessing the electrochemical performance of the transparent electrode, multiple datasets have been obtained, combined and employed to provide an overview of the relationship between processing, structure, properties, and performance.

The aim of the present work is to elucidate the mechanisms involved in the synthesis of self-assembled graphene-based hybrid nanocarbons, specifically as they relate to the understanding of the morphological and electrochemical properties, by using different statistical methods. In particular, to offer a holistic overview of the material synthesis-composition-structure-property, able to provide the fundamentals for building a tool for the predictive analytics and relationship mining of CVD-grown carbon nanostructures. Moreover, since some analytical techniques require an expert interpretation, which may prove difficult, underproductive and subjective (e.g microscopy image description, Raman spectra deconvolution) we compared the result of classifying the synthesised nanomaterials by researcher-generated datasets with different automatically generated statistical descriptors. Instead of reporting only the conditions that yielded to better-developed nanowall electrodes, all of the CVD-grown samples have been reported, including failed and partially successful ones, to better understand the weights of the process parameters on the CVD synthesis. PCA has been employed, with the purpose of highlighting the parameters that majorly affect the morphological and (electro)chemical properties of the composite, and to assess how they relate to each other.

2. Materials and methods

2.1 Electrode preparation

Carbon nanostructures were grown by microwave plasma-enhanced chemical vapour deposition (MWPECVD) on fused quartz substrates (Continental Trade Sp. z o.o., Warsaw, Poland) using a SEKI Technotron AX5400S (Tokyo, Japan) system, fed with H_2, CH_4, N_2 and B_2H_6 gases. The process duration, substrate temperature and microwave power during growth were, respectively, 15 min, 700°C, and 1300W unless explicitly stated. The effect of the substrate temperature and boron-doping in the carbon nanostructures can be found in our previous work [28]. The quartz substrates were pretreated in a H_2-rich plasma for 10 min at a microwave power of 1100 W.

2.2 Morphological and chemical characterisation

Scanning electron microscopy images were acquired via an FEI Quanta FEG 250 instrument (FEI, Hillsboro, USA), using a 15 kV beam accelerating voltage with a secondary electron–Everhart-Thornley (SE-ETD) detector working in high vacuum mode (pressure 10^{-4} Pa). Raman spectra were recorded in the range 200–3500 cm^{-1} with an integration time of 5 s (10 averages) using an argon-ion laser emitting at 514 nm. The data were smoothed (using a Savitzky-Golay method: 15 points, second polynomial order), baseline-subtracted and normalised. The electrical resistivity was measured in a four-point probe setup, with equal spacing of 1 mm, at room temperature, with a Keithley 2400 instrument. UV-visible spectra were acquired using a double beam spectrophotometer (UV-9000 Metash) in the 200–1000 nm range with a resolution of 1 nm, using deuterium and tungsten halogen lamps. Optical emission spectra were acquired by a spectrograph in the range of 250–900 nm, with an integration time of 5 seconds, 3–5 mm above the sample surface. Each presented spectrum was averaged from 20 acquisitions. Hierarchical clustering was performed with the stats package, using different datasets, as later described. The agglomeration method used was the generalising Lance-Williams formula (Ward.D2). Principal component analysis was chosen as a dimensionality reduction technique, by identifying the properties that account for the maximum variance between the samples. PCA was performed with the FactoMineR package [29] and factoExtra [30] using the R software [31]. A dissimilarity matrix between different MFs was computed using the dtw package [32]. Morphological and fractal analyses were performed on the SEM images with the open-source Gwyddion software.

2.3 Electrochemical characterisation

Cyclic voltammetry (CV) and electrochemical impedance spectroscopy (EIS) tests were performed to evaluate the electrochemical performance of the transparent composites, with the carbon nanostructure constituting the working electrode (5 mm diameter), a platinum wire as the counter electrode, and an Ag wire coated with AgCl as the reference electrode. All electrochemical tests were conducted in three different electrolytes (1M NaOH, 1M H_2SO_4 and 1M Na_2SO_4). The CV and EIS were recorded using a potentiostat-galvanostat (VMP-300, Bio-Logic, France). The CV test was carried out at scanning rates of 100, 200, 300, 400 and 500 mV/s between -0.2–0.3 V, 0.3–0.8 V, and 0.1–0.6 V in the 1M NaOH, 1M H_2SO_4 and 1M Na_2SO_4, respectively. The EIS was performed in the frequency range from 20 mHz to 200 kHz, at an open circuit potential and with an amplitude of 10 mV.

3. Theory/calculation

3.1 Minkowski functionals

The Minkowski surface, S(z), is defined as follows:

$$\mathrm{S(z)} = \frac{\mathrm{N_{bound}}(z)}{\mathrm{N}}$$

In which N_{bound} denotes the number of white-black pixel boundaries and N is the total number of pixels, as a function of threshold value *z* that divides the white pixels from the black. It is known that a single SEM micrograph is not sufficient to produce correct height (*z*-axis) information, however, since the different samples can be considered similar in terms of chemical composition and the surface homogeneous in terms of conductivity, grayscale SEM microscopy can be related to the sample height. While it is recognised that AFM is better in providing the correct representation of the sample roughness, SEM, with an SE detector, may offer a valid alternative with an enhanced resolution in the case of highly populated nanowalls. For this reason, the Mfs abscissa can be related to the relative sample's height.

The Minkowski connectivity (Euler-Poincaré Characteristic) describes the topological characteristics of structures. The structure of the pattern is calculated as follows:

$$\chi(z) = \frac{C_{white}(z) - C_{black}(z)}{N}$$

Where C_{white} and C_{black} denote the number of continuous sets of white and black pixels, respectively. A negative ordinate of the Minkowski connectivity plot indicates the presence of many disconnected flat valleys, while a positive one, the presence of disconnected, rough features. The presence of a minimum relates to the largest density of valleys and a maximum to the largest density of disconnected peaks. For a straightforward understanding of the previously Mfs, two representative BDD and BCNW SEM micrographs are reported in an explanatory representation in Figure 1a. Due to the different profile between the two nanostructures' borderline cases, with the increasing threshold level, the white and black areas vary accordingly, hence the continuous sets of white and black pixels. So it is possible to observe how the two Mfs, S(z) and χ(z) (Figure 1b,c), can be considered representative of the nanostructure morphology.

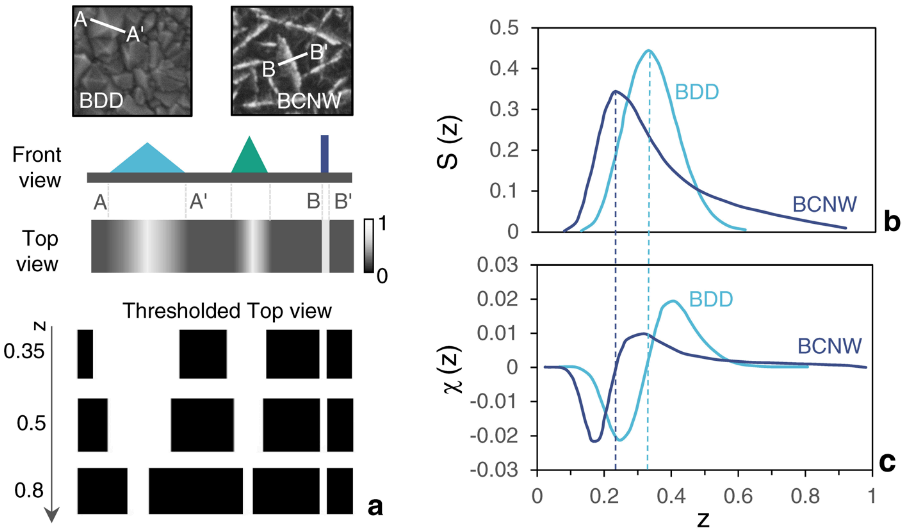

Figure 1 – (a) Schematic explanation of the Mfs for two representative cases. Representation of the (b) Minkowski surface and (c) Minkowski connectivity functions.

The boundary length, S(z), as reported in Figure 1b, tends to zero for both z→0 and z→1, reaching a maximum in between. While the BDD pattern exhibits symmetric behaviour, with a maximum at z = 0.35, the BCNW reveals an asymmetry with a maximum at z = 0.23.

In the case of the BDD, χ(z) exhibits two similar distinguishable and symmetric peaks (Figure 1c), minima and maxima within the range of 0.1<z<0.6, with an inflexion point at z ≈ 0.34. For the BCNW, χ(z) presents a sharp peak with a local minima at z ≈ 0.16 and a positively skewed peak, vanishing for z→1, indicating a highly connected structure, with an equal amount of black and white components for a longer range of z. The dissimilarity matrix was computed based on the Dynamic Time Warping (DTW) definition of a distance between MFs. DTW is a technique to find an optimal alignment between two given (time-dependent) sequences, which has recently been adapted to different types of univariate data. Examples of implementation of the DTW algorithm to spectroscopic data, which include chromatographic data [33,34], XRD diffractograms [35], and near-infrared spectroscopic data [36], have been proposed in the literature.

3.2 Fractal analysis

The power spectrum method was chosen to estimate the fractal dimension, which is based on the power spectrum dependence of fractional Brownian motion. Briefly, every line-height profile that forms the image is Fourier transformed and the power spectrum evaluated and then all of these power spectra are averaged. The fractal dimension is then evaluated from the slope β of a least-square regression line fit to the data points in the log-log plot of the power spectrum [17]. In order to measure the fractal dimensions, SEM micrographs having a magnification of 50,000x were chosen (a comparison and discussionof the different methods and magnifications is reported in the supplementary materials).

3.3 Equivalent circuit in impedance spectroscopy

The equivalent circuit (EC) adopted consists of electrolyte solution resistance (R_s), two-time constants (R and C in parallel), including two constant phase element (CPE): R_{pore}, CPE_{film} and R_{ct}, CPE_{dl}, and a Warburg element. In the high frequencies, R_{pore} and CPE_{film} are attributed to the bulk resistance and space charge bulk capacitance of the material. In the medium frequencies, R_{ct} and CPE_{dl} correspond to the charge transfer resistance and the double layer capacitance, respectively. Features such as porosity, nano-cavities, pore shape and the heterogeneous surface of the material contribute to the non-uniform distribution in the current density. These are the reasons why a constant phase element (CPE) is used to represent the deviation of the real capacitance from the capacitor ideality. The CPE is defined with the equation: $Z=Q^{-1}(i\omega)^{-n}$, where ω is the angular frequency, Q is the CPE parameter, and n is an additional parameter in the range $0<n\leq1$. In the case of a perfectly smooth surface, n tends to 1 and the CPE corresponds to an ideal capacitor. The Warburg element reflects the diffusion of electrolyte ions from the bulk of electrolyte to the surface of the electrode. A graph of the EC is presented in the following section.

4. Results

4.1 Morphological and chemical characterisation

4.1.1 UV-vis transmittance and electrical resistance

Light transmittance through the sample composite widely varies between the different samples, so the recorded spectra can provide meaningful information on the electronic transition between the energetic states. The majority of the samples exhibit an increase in absorption with a wavelength in the range of about 243–259 nm, which has been assigned to the $\pi \rightarrow \pi^*$ transition of the condensed aromatic rings in the graphene sheet [37]. A four-point probe measurement was carried out to study the effect of different synthesis conditions on the electrical resistance of the different carbon nanostructures. Due to the large measure excursion, the values have been log-transformed. Interestingly, the latter and the median optical transmittance, both in the UV and visible ranges, are inversely correlated (Figure 2). In particular, the lowest resistances belong to the CNW-like structures (blue dots) and the particular morphology results in their dramatic decrease of light transmittance.

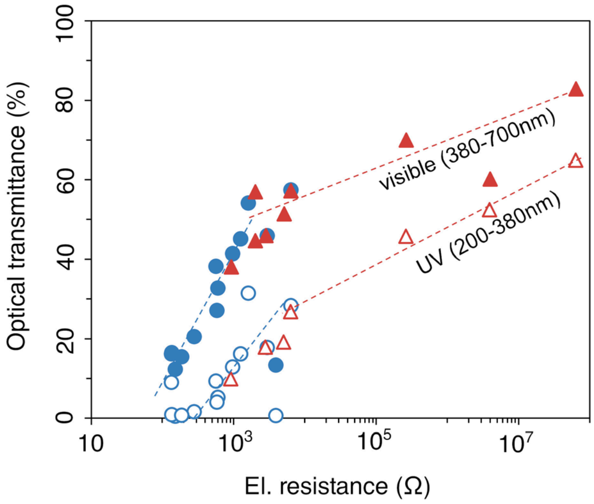

Figure 2 – Correlation between electrical resistance, measured by 4-point probe method, and optical transmittance, in the UV (solid) and visible (empty) interval, for CNW (blue dots) and other carbon nanostructures (red triangles).

4.1.2 Raman spectroscopy

The typical Raman spectra of BCNW consists of two prominent peaks in the 1300–1600 cm^{-1} range, including the D (≈1345cm^{-1}) and G (≈1590cm^{-1}) peaks. A four-peak fitting of the Raman spectrum on the BCNW layer has been performed with full Lorentz function, and it is comprised of two main peaks (D and G), and two tails, in the 1000–1750cm^{-1} interval. In the second-order Raman spectra, the main lines have been recognised as 2D and D+G bands. An analytic summary of the peak fitting position and description is reported in the supplementary materials.

It is known that the D-band is associated with the breathing mode of hexagonal carbon rings, and related to the in-plane substitutional heteroatoms, vacancies, grain boundaries, or other defects, all of which lower the crystalline symmetry [38] and its intensity is also related to the CNW size [39]. The G-band arises due to the stretching of sp^2-bonded carbon in rings and chains. It is almost independent of the excitation laser energy [38] and the half-maximum full-width ($FWHM_G$) can be considered an index of the graphitisation degree [40]. The G-band frequency (ν_G), $FWHM_G$ and peak intensity ratio of the D band to G band (I_D/I_G) correlate with the L_{wall} of the CNWs, although no strong correlation is observed in the frequency and bandwidth of the D and D′ bands [39]. The I_D/I_G peak ratio can be used to estimate the size of the sp^2 clusters through the Tuinstra-Koeing (T-K) relation [41] specifically with a λ = 514.5 nm laser excitation source:

$$\frac{I(D)}{I(G)} = \frac{C(\lambda)}{L_a}$$

where $C(514nm) \approx 4.4$ nm. This relation arises from the fact that the D peak is produced only in a small region of the nanographitic domain, near a defect or an edge. For a high defect density (<2 nm), the T-K relation fails [42].

The D, D′, 2D′, D′′, D + D′, and D + D′′ bands are activated only by defects, and these bands are absent in pristine graphene [43]; if the ratio of $I_D/I_{D'}$ is 13, it indicates the presence of sp^3-related defects, and similarly, 10.5 corresponds to hopping defects, 7 for vacancy-like defects, 3.5 for boundary-like defects, and 1.3 represents the on-site defects in graphene [44]. The interpolating line obtained by plotting I_D/I_G over $I_{D'}/I_G$ (supplementary material), well represents the majority of the samples. The slope ($I_D/I_{D'}$) is found to be equal to 5.6, suggesting the coexistence of vacancy-like and boundary-like defects. In the sample grown at a higher temperature (850°C), the $I_D/I_{D'}$ ratio is equal to 3.26, indicating a reduction of the number of vacancy-like defects. On the other hand, the sample grown with the lowest CH_4 feed and the highest B and N co-doping exhibits the presence of sp^3-related defects.

4.2 Electrochemical characterisation results

The high-frequency resistance (R_s) consists of all of the ohmic resistance in the circuit, along with the electrolyte resistance (which is constant). Due to the absence of a conductive layer underlying the carbon nanostructures, the latter ones are responsible for the current flowing towards the equivalent electrical circuit. Indeed, not only the morphology (which affects the electrode specific surface area) but the presence of hopping of carriers between the crystallites (which affects the electrical resistivity) influence R_s. For these reasons, Figure 3b reports the correlation between R_s and the sample surface resistivity, and how the increase in the crystallite size results in a reduction of the R_s [45] (Figure 3c). R_{pore} is the second resistive element and is related to the cavities within the carbon nanostructures. It is possible to observe two distinct trends when their projected boundary length is compared with the R_{pore}. (Figure 3d,e). On one side, for the other not-fully-developed carbon nanostructures, the increase of the growth in the size of the carbon isles over the quartz surface corresponds to an increase of the cavities-projected total boundary length (tpbl), which results in improved conductivity. On the other hand, for B-CNW, the cavities are represented by the space within the nanowalls; when the density of the vertical walls increases, it results in a higher tpbl of cavities, leading to a harsher path for the electrolyte to diffuse to the wall surface and a higher R_{pore}.

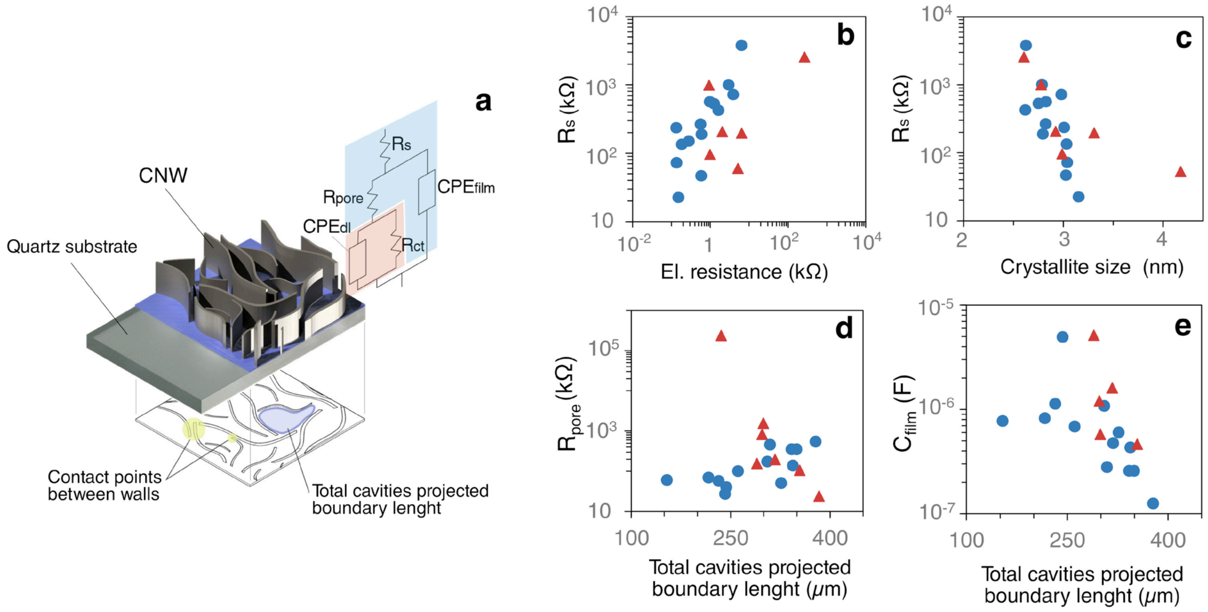

Figure 3 – (a) Schematic of the BCWN samples with the equivalent circuit (EC). Correlations between the electric resistance (b), the crystallite size (c) and the value of Rs. Correlation between the outer elements of the EC -film capacitance (d) and pore resistance (e) and the total projected cavities boundary length, estimated by SEM.

Fractal theory has been proposed by Mandelbrot [46] to describe the self-similarity of natural features, and fractal model has been adopted to describe the porosity of different materials [47]. All of the prepared samples have similar fractal dimensions with average values over all samples D = 1.94 ± 0.82.

CPE_{film} is related to the rough electrode surface. For a self-similar electrode, a few authors [48,49] have related the CPE exponential factor (n) with n_D, estimated with the following relation:

$$n_D = \frac{1}{D-1}$$

Where D is the fractal dimension of the electrode.

While the CPE_{film} is more representative of the electrode morphology, the CPE_{dl} is related to the formation of a double-layer capacitance on the interface between the electrode and its surrounding electrolyte, because of the remarked capacitive behaviour. However, differently to other authors, a negligible correlation is found between n and $\frac{1}{D-1}$ (Supplementary material).

4.3 Effect of the operational parameters on the CNW morphology

4.3.1 Effect of the CH_4 feed rate

The effect of the CH_4 feed rate on the nanostructure growth is reported in Figure 4.

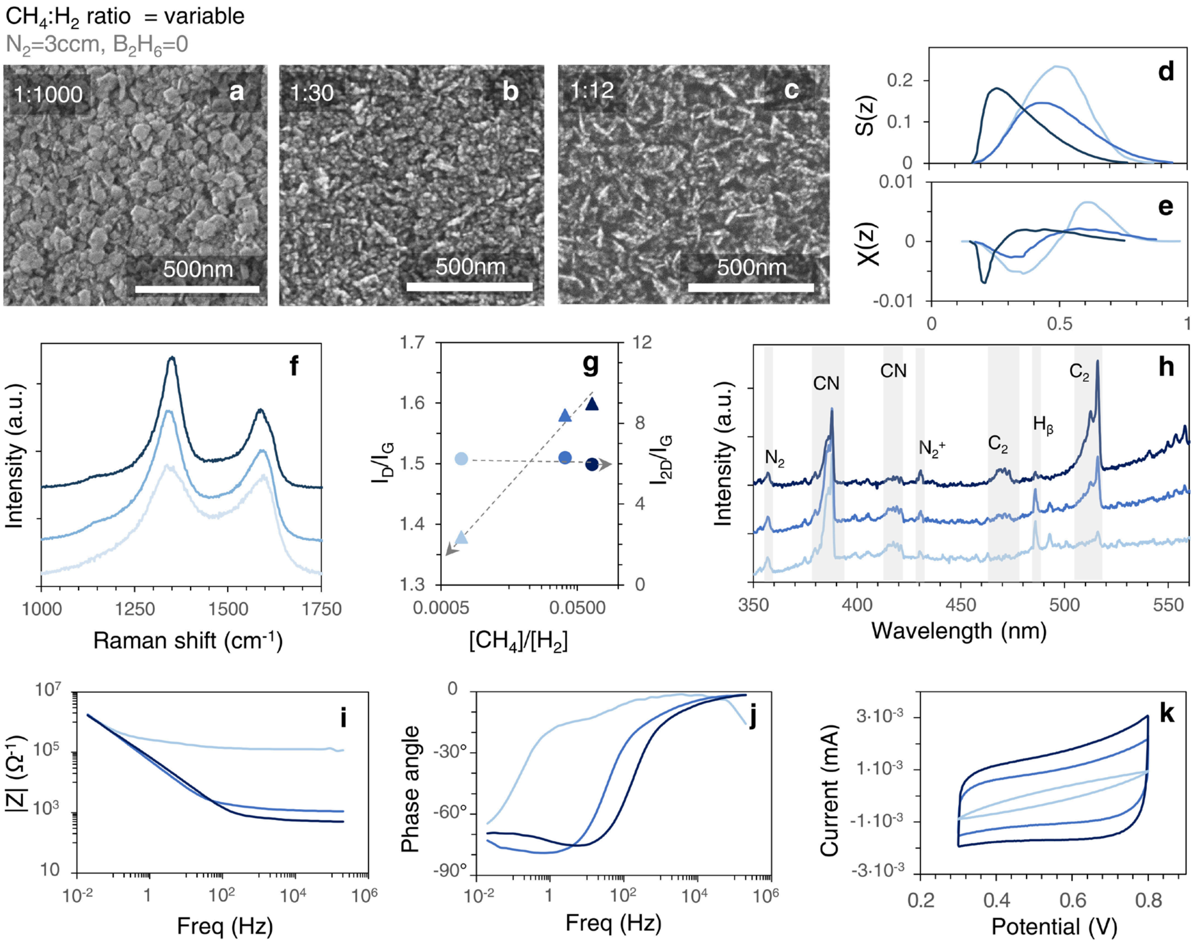

Figure 4 – (a–c) SEM, (d,e) MFs, (f) Raman spectra with relative deconvoluted (g) peak ratios, (h) optical emission spectra of the C/N/H plasma, (i,j) EIS Bode plot and (k) voltammograms of three samples grown at a variable CH_4/H_2 ratio.

From the SEM micrographs, it is possible to observe qualitatively the transition between a large-grains diamond-like structure (Figure 4a) to a more rarefract crystallinity (Figure 4b), to end up with the preferential orientating of the linear wall growth paths (Figure 4c). Of these morphologies, the Minkowski surface (Figure 4d) and connectivity (Figure 4e) have been calculated. It is possible to recognise the previously described trend in section "3.1 Minkowski functionals", discriminating between the two different structures. The Raman spectra highlight the increase of the G" and D" peaks (Figure 4f) and of the I_D/I_G ratio (Figure 4g) with the increasing CH_4 flow rate. Since the I_D/I_G ratio is inversely related to the crystallite size, it is possible to assume that the reduction of the latter indicates a higher defect concentration in the graphene lattice, dictated by the change of the plasma composition. Since the H_2 feed was kept constant, the higher CH_4/H_2 ratio results in the appearing of C_2 swan bands at ≈470 nm ($\Delta v = -1$), ≈520 nm ($\Delta v = 0$) and ≈550 nm ($\Delta v = +1$) and the lowering of the H_β peak, as shown by the peak at 486 nm in the optical emission spectra (Figure 4h). To the different nanostructures belong different electrochemical properties; in particular, the formation of smaller grains lead to the formation of porosity, recognisable by (i) the presence of a larger phase angle for the time constant having frequency at ≈100Hz, and by (ii) a new time constant appearing at high frequencies, absent for the sample with large particles (Figure 4i–j). The value of |Z| for high frequencies is comparable for the samples synthesised at higher CH_4, while it is two orders of magnitude greater for the diamond-like sample which is characterised by a different slope of the transition region between the two asymptotic limits. The development of an inter-wall porosity also results in the increase of the composite specific capacitance, as shown by the CV voltammograms in Figure 4k.

4.3.2 Effect of the N_2/CH_4 ratio

The effect of the nitrogen concentration within the reactor varied in the 1:80–1:5 range against the constant CH_4 concentration. SEM micrographs of the different nanostructures obtained are reported in Figure 5a–c. In this case too, the Minkowski functionals discriminate between the different nanostructure types (Figure 5d,e).

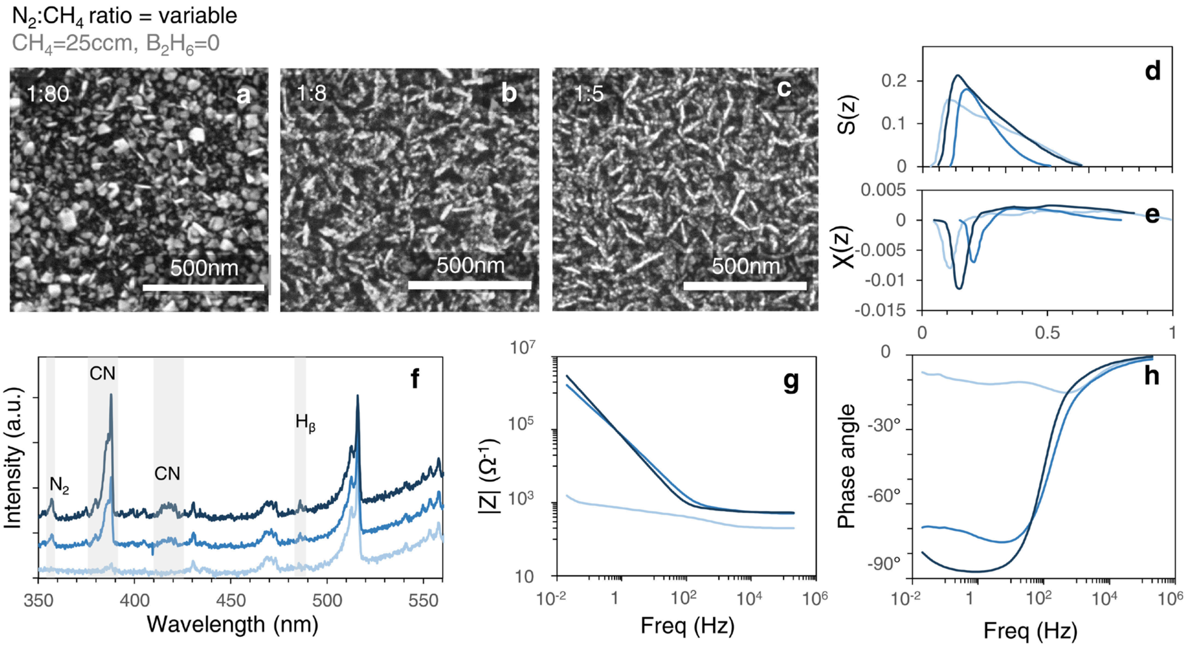

Figure 5 – (a–c) SEM, (d,e) MFs, (f) optical emission spectra of the C/N/H plasma, (g,h) EIS Bode plot of three samples grown at a variable N2/CH4 ratio.

The high CH_4 flow, accompanied by a low N_2 stream, results in an excess of plasma-initiated carbon-containing species which produce a disordered layer of sp^2-rich agglomerations of nanoparticles, characterised by larger graphitic domains. By increasing the concentration of the nitrogen precursor, CN radicals are formed, which actively participate in the nanowall growth, as shown by the bands at 385 nm (N_2) and CN bands at 386 nm and 418 nm (Figure 5f). The increasing content of nitrogen species results in an obvious alteration of the plasma chemistry, at the expenses of the C_2 band at 516.3 nm ($D^3\Pi_g \rightarrow A^3\Pi_u$). While the sample grown with the lowest N_2 concentration may appear similar in morphology to the previous DLC sample (Figure 4a), they largely differ, since the impedance modulus ranges between 1.5–0.2 × 10^3 Ω^{-1} (Figure 5g), exhibiting a maximum phase angle of-20° and a quasi-resistive behaviour for the range of frequencies considered (Figure 5h). With the increasing N_2 concentration, so enhancing the vertical arrangement, it is possible to distinguish two time constants in the Bode plot for the 10^{-1} and 10^2 Hz frequencies.

4.3.2 Effect of the N_2/CH_4 ratio with B_2H_6

The low content of CH_4 and the co-presence of N_2 led to defective nucleation (Figure 6a), while, with higher B-doping levels, it is possible to control the CNW density (Figure 6b,c) and facilitate initial nucleation. With increasing both the CH_4 and N_2 concentrations, the average CNW length decreases, leading to a more fragmented morphology (Figure 6d–f).

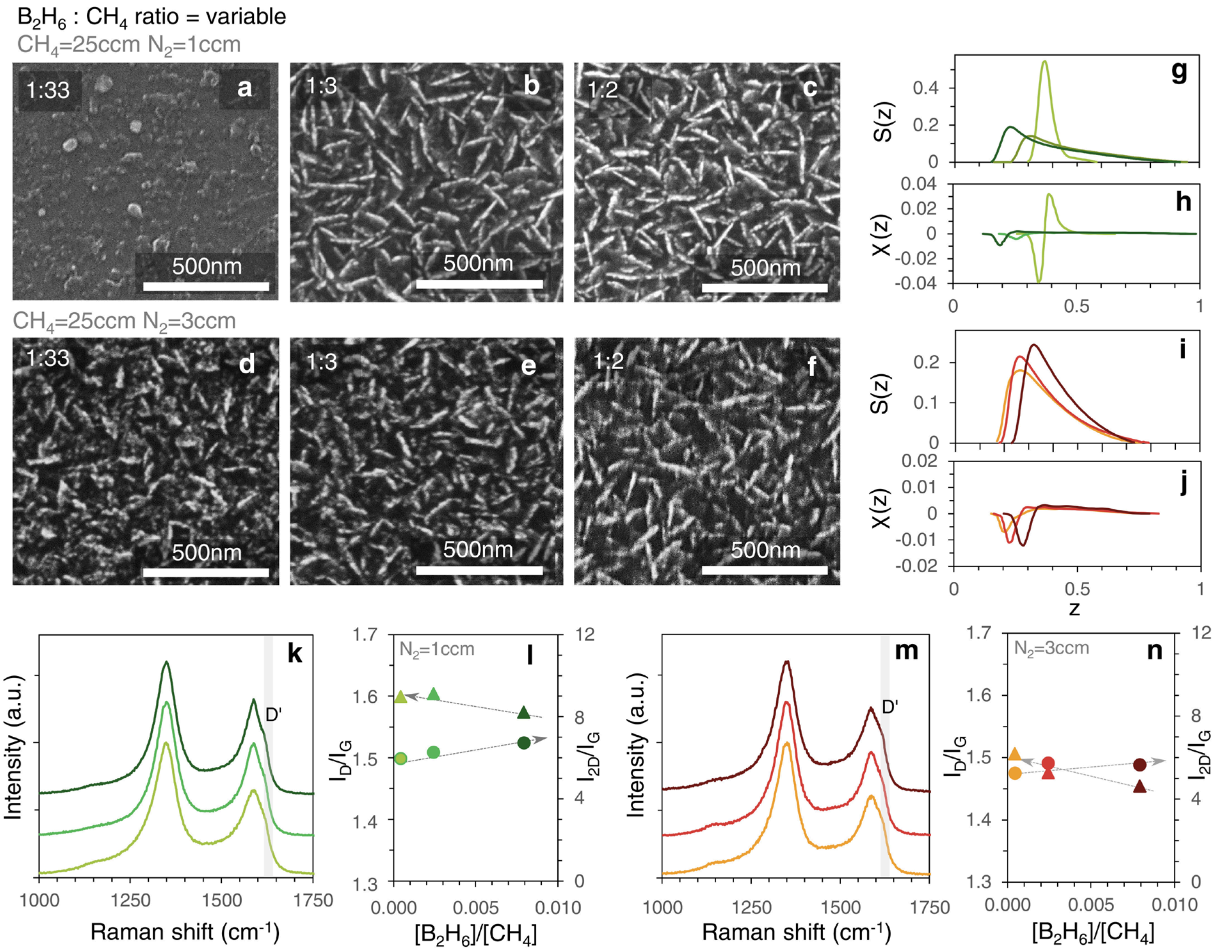

Figure 6 – (a–f) SEM, (g–j) MFs, (k,m) Raman spectra, (l,n) I_D/I_G and I_{2D}/I_G ratios of three samples grown at a variable B_2H_6/CH_4 ratio.

The intensity of peaks in a Minkowski surface functional monotonically increase as a function of the B_2H_6 content, while the peak position follows different behaviours for the two sets: it decreases with B_2H_6 for the set with low CH_4 and N_2 feeds (Figure 6g), while it increases for the high-feed set (Figure 6i). This is similar for the Minkowski connectivity (Figure 6h,j). In both sets, the B-incorporation led to the increased intensity of the D' band [14], attributable to the high level of disorder (Figure 6k,m), to the decrease of the I_D/I_G ratio and the increase of the I_D/I_{2D} ratio (Figure 6l,n).

4.3.3 Effect of the B_2H_6/N_2 ratio

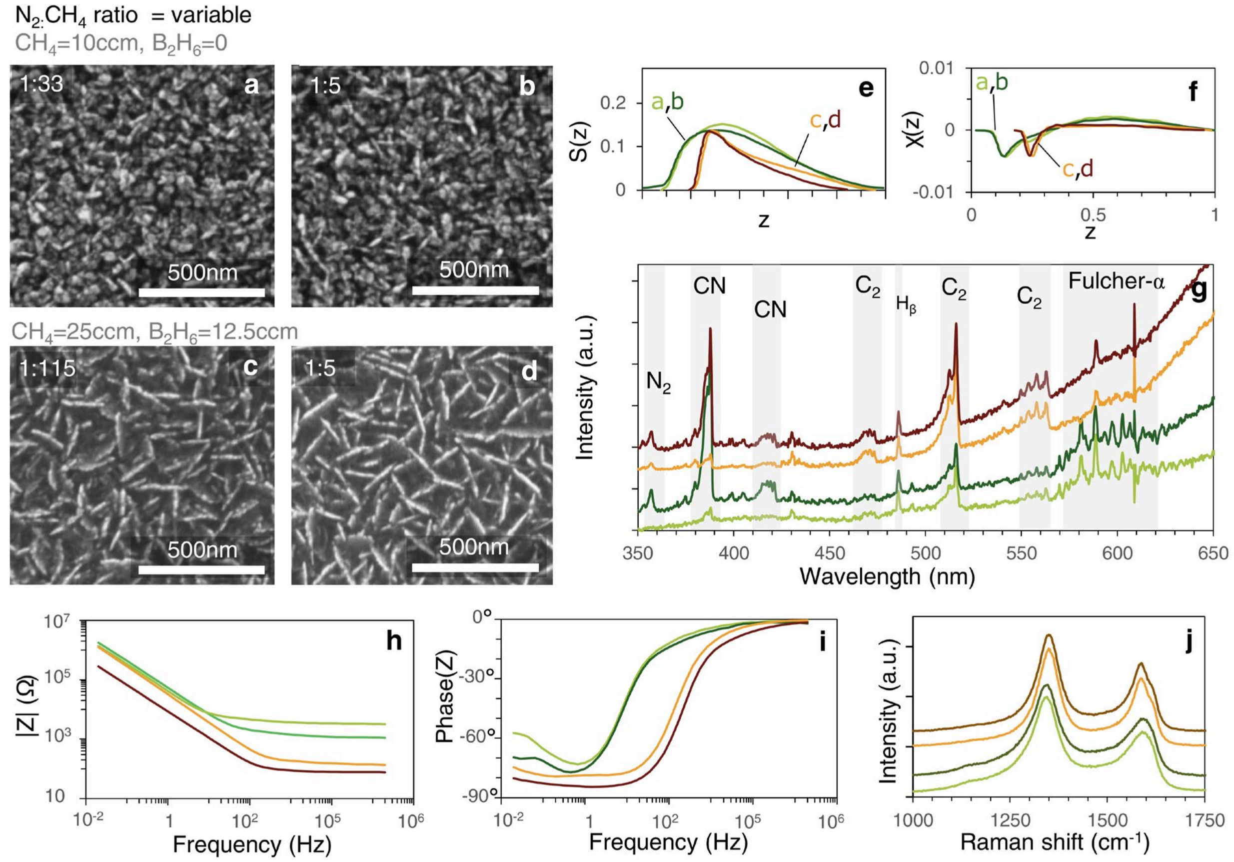

Figure 7 – (a–d) SEM, (e,f) MFs, (g) optical emission spectra of the C/N/H plasma, (h,i) EIS Bode plot, (j) Raman spectra of three samples grown at different B-dopings and a variable N_2/CH_4 ratio.

The role of the CN radicals in the nanowall growth is secondary to that provided by the B-radicals or by the CH_4 feed. Figure 7g reports how, despite the higher peaks related to the presence of CN radicals in the sample with the lowest CH_4 concentration, the formation of the wall-like structure is inhibited. The low reactivity can also be highlighted by the low degree of dissociation of the hydrogen, as pointed to the ratio between the H_γ (434 nm) and the Fulcher-α (560–630 nm) [50], since for the B-doped samples represented in Figure 7c,d, grown in excess of CH_4, the H_γ is slightly higher and the Fulcher-α spectra is not appreciable, compared to the other two samples reported in Figure 7a,b. Moreover, the presence of C_2 radicals seems to contribute to the effective CNW development, as reported by the C_2 peaks (≈470 and 560 nm) and also confirmed by other authors [51].

4.4 Relationship mining by multivariate data analysis

From the entire dataset, 49 variables were selected to perform the multivariate data analysis. Five variables (process duration, N_2/CH_4, B_2H_6/CH_4, B_2H_6/N_2, CH_4/H_2 ratios) are representative of the synthesis parameters. Electrical resistivity, measured with a 4-point probe method, has been log-transformed and indicated as log(R). The median value of the light transmittance has been calculated and differed between the UV (200–380 nm) and visible (380–740 nm) components. The median of the nanostructure main dimension has been manually measured from the SEM micrographs and indicated as ℓ. Of the deconvoluted Raman spectra, the peak positions, FWHMs and relevant ratios between the peak heights have been reported. From the electrochemical characterisation, the log-scaled values of the resistance, capacitance and CPE exponential factor (n) for the different components of the EIS equivalent circuit, jointly with the capacitance value estimated by CV, in acidic, neutral and basic electrolyte have been included. Moreover, from the SEM images, 7 different parameters have been obtained, using different analysis techniques.

In order to introduce the Mfs within the analysis, the peak-to-valley distance (M_c) of the Minkowski connectivity was calculated while, the curve kurtosis (M_{skurt}), skewness (M_{ssk}), and ordinate at the peak maximum (M_{sz}) of the Minkowski surface were computed. Additionally, the total projected boundary length (*tpbl*), as defined in Figure 3a, and the fractal dimension, D, have been included to the second dataset, with the manually computed CNW length (ℓ). Prior to PCA, to avoid the potential pitfall of including these correlated variables (since they were all obtained from the same SEM micrography analysis), the Spearman correlation coefficient was evaluated (Figure 8a). The highest correlation found was between the Minkowski surface curve kurtosis and skewness. The first two dimensions express 49.92% of the total dataset inertia and the analysis was restricted to the first 3 axes (Figure 8b, Supplementary materials).

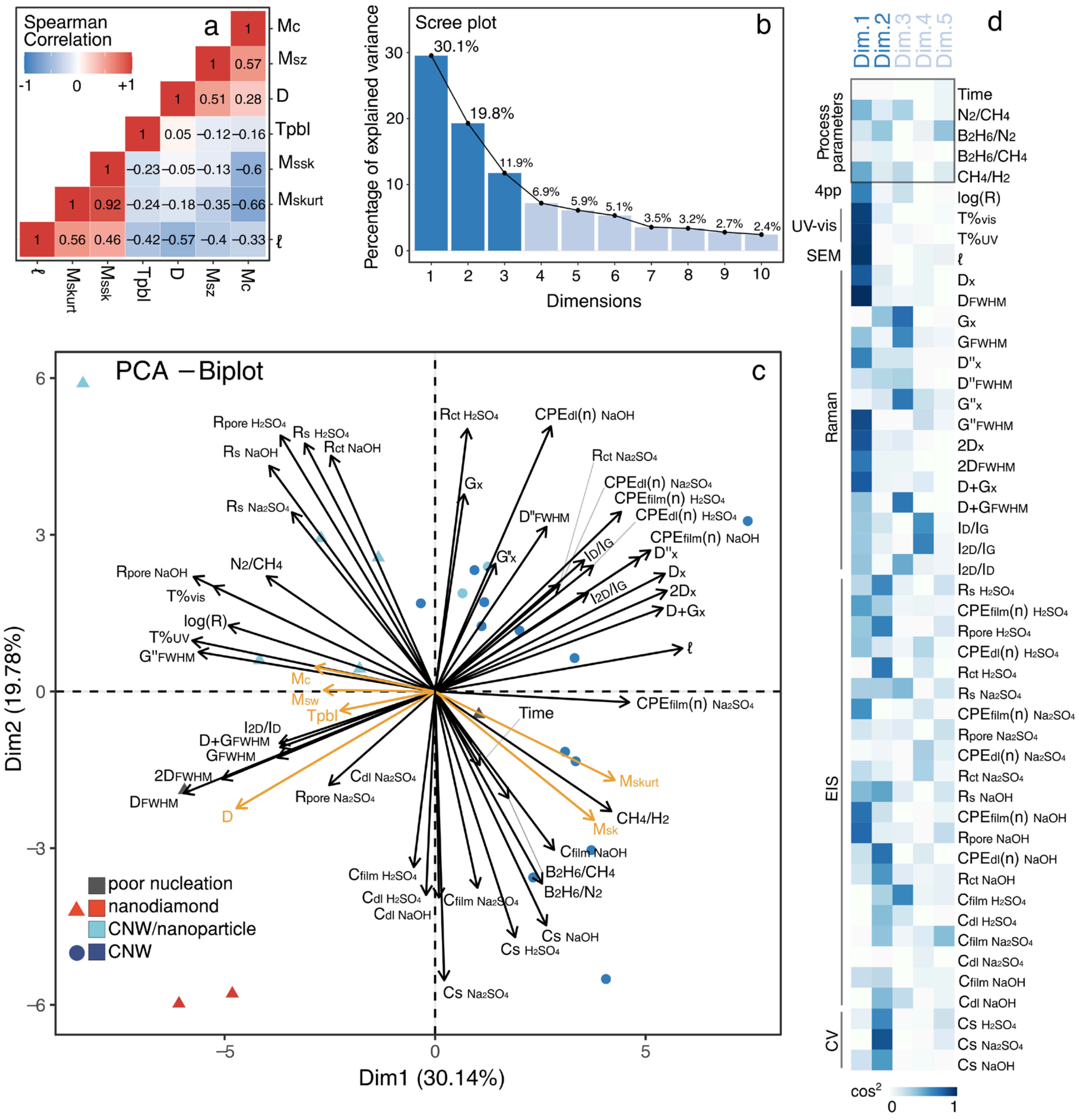

Figure 8 – (a) Correlation between the SEM-derived parameters (b) Scree plot, (c) Principal Component analysis and (d) cos² heatmap for the first five dimensions.

Figure 8c reports the samples (observations) projected into the new reference system (represented by the first two new dimensions, which are a linear correlation of the previous variables) and it is possible to observe a clear division between the CNW samples and the other carbon nanostructured samples, corresponding to the first dimension (Dim1). Samples having a positive abscissa are characterized by a CNW-like morphology, differently from the other carbon nanostructures placed on the negative part of the axis. This qualitative descriptor could therefore summarise itself in the first dimension. According to the variables close to the abscissa, the CNWs are well described by the shift of D+G, 2D, D, D'' peak centres toward higher values and, obviously, by the nanowall length. Among all of the Lorentzian-fitted Raman peak centres, D_x, and $D+G_x$ are the most representative, as they display the highest standard deviations. Light transmittance and electrical resistivity are negatively correlated, and they are higher for decreasing CNW maze-like morphology. The increasing capacitive behaviours of the CPE_{film} (the exponential factors) are correlated with all of the parameters characterising a well-developed CNW structure, such as ℓ, D_x, $D+G_x$, and I_D/I_G, and negatively correlated with the FWHM of D, 2D and G''.

The second dimension (Dim2) opposes samples characterised by high values of electrolyte resistance (R_s, R_{ct} and R_{pore}), high N_2/CH_4 and low CH_4/H_2 ratios, exhibiting a nanodiamond-like morphology (characterised by strongly negative coordinates on the axis) to other carbon nanostructures, different from CNW, resulting from the higher value of the N/C ratio, generally with a low B doping. The process variables showing significant correlations are CH_4/H_2, N_2/CH_4, and B_2H_6/N_2. In particular, the specific capacitances, measured by CV in different electrolytes, and the capacitance of the CPE_{film} are correlated with the B_2H_6/N_2 ratios and with the position of the Raman G-peak (G_x). It has been reported that a positive shift of the G-peak position can be due to doping, synthesis temperature, uniaxial [52] and biaxial [53] strains and to an increase of the sp^3-bonded carbon content. Since the G-peak position and I_D/I_G ratio are inversely correlated with the presence of sp^3-bonded carbon [54], the increase of sp^2-coordinated atoms is beneficial to the charge storage ability, while the sp_3-bonded carbon is beneficial to the charge transfer resistance enhancement [55].

The third dimension accounts for 11.9% of the total variance and oppose the B_2H_6/N_2 to the I_D/I_{2D} ratio. The significant variables have been reported in the supplementary materials.

4.5 Hierarchical clustering of self-assembled carbon nanomaterials

Identification of clusters with similar properties, between the different samples, was performed by hierarchical clustering for all single datasets (process, optoelectrical, electrochemical, Raman-derived and Mfs-derived). A detailed and schematic explanation of how the data was treated is reported in the supplementary materials.

Dissimilarity matrices for the Minkowski surface and Minkowski connectivity were computed based on the Dynamic Time Warping (DTW) definition of a distance between SEM-derived Mfs. Hierarchical clustering was then performed using the Ward (squared) method. For both dendrograms, it is possible to observe the definition of two principal clusters (Figure 9a). The first represented by all of the CNW structures and the second by different nanostructures (enclosed into the dashed rectangle). Within the CNW cluster, it is possible to distinguish how the different Mfs work: high dissimilarity in the Minkowski surface potential results in samples sharing similar aerial features, such as discontinuity arising to the presence of nanoparticle agglomerates, while the Minkowski connectivity clustering describes the nanowall development, in terms of uniformity and length (Figure 9a,b).

A similar approach, using DTW, was applied to the Raman spectra, and the clustering results were compared with the deconvoluted Raman one. Baker's Gamma index was chosen as the cluster correlation method, since this measure is not affected by the height of a branch but only by its relative position compared with other branches, and p-values were calculated by the permutation method. The results are reported in Figure 9c; values range between -1 and +1, with values close to zero corresponding to dendrograms which are not statistically similar. Non-significant indexes have been shaded. The highest correlation belongs to the two MFs, since both are derived from the same SEM image analysis. Interestingly, a Gamma index equal to 0.45 has been obtained for the two Raman datasets, which suggests how the DTW can be used to support the manual time-consuming spectra deconvolution method. Moreover, it is possible to observe that the morphological dataset is well correlated with the deconvoluted Raman dataset and the electrochemical with the Mfs. It is worth pointing out that, while the DTW dissimilarity matrix has been directly computed using the raw spectra, for the deconvoluted one, five different distance methods have been computed (three metric-based and two statistical) on the deconvoluted peaks (Supplementary materials).

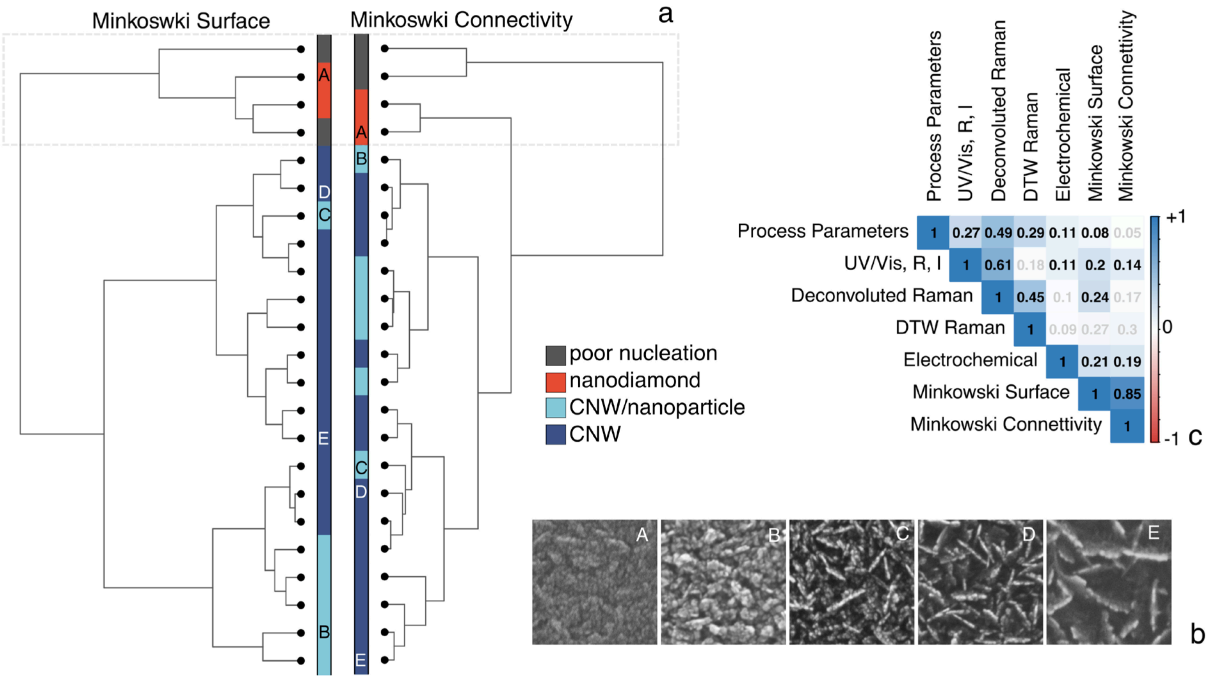

Figure 9– (a) Comparison of the result of hierarchical clustering of two datasets comprising the same samples. Representative SEM micrographs (1x1µm) of the samples (b) are reported along the dendrograms. (c) Correlation (gamma index) between different clusters.

5. Discussion

5.1 Parameters affecting CNW nucleation and growth

A few authors have pointed out that the presence of an amorphous and graphitic carbon layer, due to the rapid catalytic decomposition of carbon precursor on the metal surface [56], is the reason for the formation of defects, which will constitute preferable nucleation points for the subsequent CNW growth [57]. While this reason can explain the difficulty encountered by other authors in growing CNWs on dielectric surfaces [58], for others, the CNW growth mechanism was similar, but slower [59]. Yang et al. describe the graphene film formed on a SiO_2 surface different from the one deposited on Cu or Ni by conventional CVD, consisting of polycrystalline graphene, characterised by a low degree of crystallinity [9]. Although nucleation on a dielectric surface takes place with more effort, in our study, we highlighted that different parameters equally concur:

- CH_4:H_2 ratio: To form the carbon buffer on the substrate surface, the H_2 concentration should be controlled, since H atoms are effective etchants for a-C, sp^2 and sp^3 hybridised carbon, which would reduce the number of defects effective for the wall growth. Figure 4 reports the growth of diamond-like particles for a low CH_4:H_2 ratio. With the increasing CH_4 content, the signal from the CN radicals slightly decreases, while the C_2 dimer concentration increases (which play a crucial role in CNW nucleation [51]), together with the formation of unsaturated radicals such aromatic species and chains, reflected in an increasing I_D/I_G ratio.
- N_2, B_2H_6 concentrations. The dangling bonds produced by the incorporation of nitrogen are not the only defect which can be exploited to enhance nucleation. Indeed, while the contribution of CN radicals in the CNW growth is essential in the absence of other dopants (Figure 5), the copresence of BH_x radicals plays a predominant role in controlling CNW formation (Figure 6 and Figure 7). We reported that the strong influence of BH_x is mainly related to the re-nucleation and twinning surface process, which results in nanowall shortening with the increasing boron concentration [14], and it has also been observed with the decrease of the crystallite size. In the PCA representation (Figure 8), the B_2H_6/N_2 ratio is positively correlated with the increase of the sample specific capacitance, as support for the previous finding, which is a direct consequence of the nanowall shortening and overcrowding. Not by chance, also the process duration (directly proportional to the CNW thickness) and the CH_4/H_2 ratio (previously discussed) belong to the same group characterised by a dense CNW morphology. However, an increase in the N_2/CH_4 ratio does not directly imply faster wall growth. The CN radicals provide valuable help at a low concentration while, at a higher concentration, the wall growth process is directed by the formation and agglomeration of carbon nanosized-clusters, resulting in thicker and irregularly shaped structures.

5.2 Electrochemical behaviour of the self-assembled carbon nanoelectrodes

Three different typical electrochemical behaviours emerge from the PCA.

- The most evident is highlighted by the first dimension, and is the differentiation between a resistive (negative abscissa) and a capacitive behaviour (positive abscissa), which is consistent with the transition between diamond-like and CNW-like nanostructure. While the first type is characterised by a single time constant at low frequencies in EIS, the transition to a CNW-like morphology led to the formation of at least two time constants at medium-high ones, due to the CNW maze-like structure, leading to a harsher path for the electrolyte, which are possible to tune by varying process parameters, such as B-doping and temperature.
- The second differentiation takes place within the CNW samples and is representative of the CNW morphology and density, visually represented by the ordinate of the principal component analysis plot. Two phenomena simultaneously occur: the interspace between vertical nanosheets has the function of an "ion-reservoir", which contributes to the capacitive behaviour, well described by the CPE_{film}, and the increase in extension of the wall surfaces, which, considered as single "nanoelectrodes", results in a decrease of the resistive character. These two aspects are well represented in the PCA plot (Figure 8), as well as the clustering of different samples. The specific capacitance, time constants and charge transfer resistance are functions of the electrolyte.

5.3 Multivariate data analysis and clustering techniques

A principal component analysis was performed to identify the important factors affecting the sample characteristic, as well as to explore possible relationships between different samples and process parameters. The first component accounted for different parameters, which successfully discriminate the different carbon nanostructures, highlighting which process parameters affect the sample morphology and electrochemical behaviour.

The fractal dimension of the CVD-grown nanostructure, derived by SEM images, was found to be inversely correlated to its capacitive behaviour, as suggested by other authors, and to the graphene crystallite size, as shown by the correlation with the FWHMs of the D, G and 2D bands [60] (Figure 8). In other words, the decrease of the average crystallite size results in a greater fractal dimension.

For the first time, the Dynamic Time Warping algorithm was applied to SEM-derived Minkowski Functionals in order to effectively classify the carbon nanostructures grown by CVD. Both procedures derived from each Mfs correctly classified the CNW structures from the other poorly nucleated and nanodiamond-like samples. The Minkowski surface better performs clustering considering the overall nanomaterial morphology, while Minkowski Connectivity focusses on the nanowall length and (dis)continuity.

6. Conclusion

This study provides the basis for the analysis of different material systems and their respective data features by comparing dissimilarity measures between different datasets. The synergistic approach of using data obtained from different analytic, spectroscopic, imaging analysis and multivariate statistical methods allowed the underlying relations of CVD-grown nanomaterials to be extracted and better understood. The application of different algorithms to the imaging data (e.g. Minkowski functionals, fractal dimension analysis), aimed at the extraction of specific features, and their implementation into multivariate statistical methods paves the way for building a tool for the predictive analytics and relationship mining of CVD-grown carbon nanostructures, substituting it for subjective data interpretation and speeding up data analysis.

In particular, future work will investigate the possibility of applying the described methods to different datasets and materials, and further, to include various characterisation techniques and to interrelate the processing-structure-properties- performance paradigm.

Acknowledgements

M. P.: Conceptualization, Investigation, Formal analysis, Writing - Original Draft. M. F.: Methodology, Validation, Writing - Review & Editing. P.J.: Methodology, Investigation, Writing - Original Draft. J.K.: Investigation, Data Curation. R.B.: Conceptualization, Writing - Review & Editing, Project administration, Supervision

Funding

This research was supported by the Polish National Agency for Academic Exchange (NAWA), under the Ulam program, Agreement no. PN/ULM/2019/1/00061/DEC/1 (M.Pierpaoli) and by the i-CLARE project (NOR/POLNOR/i-CLARE/0038/2019).

Data availability

The raw/processed data required to reproduce these findings cannot be shared at this time as the data also forms part of an ongoing study.

References

[1] G.B. Olson, Brains of Steel: Mind Melding with Materials, Int. J. Eng. Educ. 17 (2001) 468–471.

[2] A. Dettlaff, P. Jakóbczyk, M. Ficek, B. Wilk, M. Szala, J. Wojtas, T. Ossowski, R. Bogdanowicz, Electrochemical determination of nitroaromatic explosives at boron-doped diamond/graphene nanowall electrodes: 2,4,6-trinitrotoluene and 2,4,6-trinitroanisole in liquid effluents, J. Hazard. Mater. 387 (2020) 121672. https://doi.org/10.1016/j.jhazmat.2019.121672.

[3] M. Brodowski, M. Kowalski, M. Skwarecka, K. Pałka, M. Skowicki, A. Kula, T. Lipiński, A. Dettlaff, M. Ficek, J. Ryl, K. Dziąbowska, D. Nidzworski, R. Bogdanowicz, Highly selective impedimetric determination of Haemophilus influenzae protein D using maze-like boron-doped

carbon nanowall electrodes, Talanta. 221 (2021). https://doi.org/10.1016/j.talanta.2020.121623.
[4] M. Pierpaoli, P. Jakobczyk, M. Sawczak, A. Łuczkiewicz, S. Fudala-Książek, R. Bogdanowicz, Carbon nanoarchitectures as high-performance electrodes for the electrochemical oxidation of landfill leachate, J. Hazard. Mater. 401 (2021) 123407. https://doi.org/10.1016/j.jhazmat.2020.123407.
[5] S. Ghosh, G. Sahoo, S.R. Polaki, N.G. Krishna, M. Kamruddin, T. Mathews, Enhanced supercapacitance of activated vertical graphene nanosheets in hybrid electrolyte, J. Appl. Phys. 122 (2017) 214902. https://doi.org/10.1063/1.5002748.
[6] Y. Wu, B. Yang, B. Zong, H. Sun, Carbon nanowalls and related materials . J Mater Chem 14 : 469-477 Carbon nanowalls and related materials, (2004) 469–477. https://doi.org/10.1039/b311682d.
[7] J. Nong, W. Wei, X. Song, L. Tang, J. Yang, T. Sun, L. Yu, W. Luo, C. Li, D. Wei, Direct growth of graphene nanowalls on silica for high-performance photo-electrochemical anode, Surf. Coatings Technol. 320 (2017) 579–583. https://doi.org/10.1016/j.surfcoat.2016.10.092.
[8] L. Cui, K. Cui, H. Ci, K. Zheng, H. Xie, X. Gao, Y. Zhang, Z. Liu, Transparent electrothermal heaters based on vertically-oriented graphene glass hybrid materials, Nanomaterials. 9 (2019) 1–10. https://doi.org/10.3390/nano9040558.
[9] C. Yang, H. Bi, D. Wan, F. Huang, X. Xie, M. Jiang, Direct PECVD growth of vertically erected graphene walls on dielectric substrates as excellent multifunctional electrodes, J. Mater. Chem. A. 1 (2013) 770–775. https://doi.org/10.1039/c2ta00234e.
[10] X. Feng, Z. He, W. Zhu, M. Zhao, Z. Liu, S. Yang, S. Tang, Q. Guo, Z. Jin, D. Chen, G. Ding, G. Wang, Perovskite quantum dots integrated with vertically aligned graphene toward ambipolar multifunctional photodetectors, J. Mater. Chem. C. (2021). https://doi.org/10.1039/d0tc04932h.
[11] O. Bayram, A study on 3D graphene synthesized directly on Glass/FTO substrates: Its Raman mapping and optical properties, Ceram. Int. 45 (2019) 16829–16835. https://doi.org/10.1016/j.ceramint.2019.05.224.
[12] J.L. Qi, X. Wang, J.H. Lin, F. Zhang, J.C. Feng, W.D. Fei, Vertically oriented few-layer graphene-nanocup hybrid structured electrodes for high-performance supercapacitors, J. Mater. Chem. A. 3 (2015) 12396–12403. https://doi.org/10.1039/c5ta01330e.
[13] N. M. Santhosh, G. Filipič, E. Kovacevic, A. Jagodar, J. Berndt, T. Strunskus, H. Kondo, M. Hori, E. Tatarova, U. Cvelbar, N-Graphene Nanowalls via Plasma Nitrogen Incorporation and Substitution: The Experimental Evidence, Nano-Micro Lett. 12 (2020). https://doi.org/10.1007/s40820-020-0395-5.
[14] M. Sobaszek, K. Siuzdak, J. Ryl, M. Sawczak, S. Gupta, S.B. Carrizosa, M. Ficek, B. Dec, K. Darowicki, R. Bogdanowicz, Diamond Phase (sp3-C) Rich Boron-Doped Carbon Nanowalls (sp2-C): Physicochemical and Electrochemical Properties, J. Phys. Chem. C. 121 (2017) 20821–20833. https://doi.org/10.1021/acs.jpcc.7b06365.
[15] M. Pierpaoli, M. Ficek, M. Rycewicz, M. Sawczak, J. Karczewski, M. Ruello, R. Bogdanowicz, Tailoring Electro/Optical Properties of Transparent Boron-Doped Carbon Nanowalls Grown on Quartz, Materials (Basel). 12 (2019) 547. https://doi.org/10.3390/ma12030547.
[16] E. Strelcov, A. Belianinov, B.G. Sumpter, S. V. Kalinin, Extracting physics through deep data analysis, Mater. Today. 17 (2014) 416–417. https://doi.org/10.1016/j.mattod.2014.10.002.
[17] W. Zahn, A. Zösch, Characterization of thin-film surfaces by fractal geometry, Fresenius. J. Anal. Chem. 358 (1997) 119–121. https://doi.org/10.1007/s002160050360.
[18] I. Levchenko, J. Fang, K. (Ken) Ostrikov, L. Lorello, M. Keidar, Morphological Characterization of Graphene Flake Networks Using Minkowski Functionals, Graphene. 05 (2016) 25–34. https://doi.org/10.4236/graphene.2016.51003.
[19] F. De Nicola, P. Castrucci, M. Scarselli, F. Nanni, I. Cacciotti, M. De Crescenzi, Multi-fractal hierarchy of single-walled carbon nanotube hydrophobic coatings, Sci. Rep. 5 (2015) 1–9. https://doi.org/10.1038/srep08583.
[20] V. V. Mitic, H.J. Fecht, M. Mohr, G. Lazovic, L. Kocic, Exploring fractality of microcrystalline diamond films, AIP Adv. 8 (2018). https://doi.org/10.1063/1.5034469.
[21] Q.F. Hou, X.C. Lu, X.D. Liu, B.X. Hu, J.Q. Cui, J. Shen, The surface fractal investigation on carbon nanotubes modified by the adsorption of poly(acrylic acid), Surf. Coatings Technol. 190 (2005) 394–399. https://doi.org/10.1016/j.surfcoat.2004.03.016.
[22] L.L.G. Silva, N.G. Ferreira, M.E.R. Dotto, M.U. Kleinke, The fractal dimension of boron-doped diamond films, Appl. Surf. Sci. 181 (2001) 327–330. https://doi.org/10.1016/S0169-4332(01)00429-9.
[23] C.C. Chou, H.H. Lin, Fractal dimension and surface topography on the diamond deposition of

seeded WC-Co substrates, J. Appl. Phys. 107 (2010). https://doi.org/10.1063/1.3359657.
[24] ŢĂlu, M. Bramowicz, S. Kulesza, A. Ghaderi, V. Dalouji, S. Solaymani, M.F. Kenari, M. Ghoranneviss, Fractal features and surface micromorphology of diamond nanocrystals, J. Microsc. 264 (2016) 143–152. https://doi.org/10.1111/jmi.12422.
[25] N. Bonnet, Multivariate statistical methods for the analysis of microscope image series: Applications in materials science, J. Microsc. 190 (1998) 2–18. https://doi.org/10.1046/j.1365-2818.1998.3250876.x.
[26] E. Widjaja, M. Garland, Reverse engineering of multi-layer films, Mater. Today. 14 (2011) 114–117. https://doi.org/10.1016/S1369-7021(11)70061-X.
[27] K. Rajan, Materials informatics, Mater. Today. 8 (2005) 38–45. https://doi.org/10.1016/S1369-7021(05)71123-8.
[28] M. Pierpaoli, M. Ficek, M. Rycewicz, M. Sawczak, J. Karczewski, M. Ruello, R. Bogdanowicz, Tailoring Electro/Optical Properties of Transparent Boron-Doped Carbon Nanowalls Grown on Quartz, Materials (Basel). 12 (2019) 547. https://doi.org/10.3390/ma12030547.
[29] S. Lê, J. Josse, F. Husson, FactoMineR: An R package for multivariate analysis, J. Stat. Softw. 25 (2008) 1–18. https://doi.org/10.18637/jss.v025.i01.
[30] A. Kassambara, F. Mundt, Factoextra: extract and visualize the results of multivariate data analyses, R Packag. Version. 1 (2017) 2017.
[31] R Core Team, R: A language and environment for statistical computing., (2013).
[32] T. Giorgino, Computing and Visualizing Dynamic Time Warping Alignments in R: The dtw Package, J. Stat. Software; Vol 1, Issue 7 . (2009). https://www.jstatsoft.org/v031/i07.
[33] G. Tomasi, F. Van Den Berg, C. Andersson, Correlation optimized warping and dynamic time warping as preprocessing methods for chromatographic data, J. Chemom. 18 (2004) 231–241. https://doi.org/10.1002/cem.859.
[34] N.P.V. Nielsen, J.M. Carstensen, J. Smedsgaard, Aligning of single and multiple wavelength chromatographic profiles for chemometric data analysis using correlation optimised warping, J. Chromatogr. A. 805 (1998) 17–35. https://doi.org/10.1016/S0021-9673(98)00021-1.
[35] Y. Iwasaki, A.G. Kusne, I. Takeuchi, Comparison of dissimilarity measures for cluster analysis of X-ray diffraction data from combinatorial libraries, Npj Comput. Mater. 3 (2017) 1–8. https://doi.org/10.1038/s41524-017-0006-2.
[36] E.N.M. Van Sprang, H.J. Ramaker, J.A. Westerhuis, A.K. Smilde, S.P. Gurden, D. Wienke, Near-infrared spectroscopic monitoring of a series of industrial batch processes using a bilinear grey model, Appl. Spectrosc. 57 (2003) 1007–1019. https://doi.org/10.1366/000370203322258986.
[37] G. Carotenuto, A. Longo, S. De Nicola, C. Camerlingo, L. Nicolais, A simple mechanical technique to obtain carbon nanoscrolls from graphite nanoplatelets, Nanoscale Res. Lett. 8 (2013) 1–6. https://doi.org/10.1186/1556-276X-8-403.
[38] Z.H. Ni, H.M. Fan, Y.P. Feng, Z.X. Shen, B.J. Yang, Y.H. Wu, Raman spectroscopic investigation of carbon nanowalls, J. Chem. Phys. 124 (2006) 204703. https://doi.org/10.1063/1.2200353.
[39] S. Kurita, A. Yoshimura, H. Kawamoto, T. Uchida, K. Kojima, M. Tachibana, P. Molina-Morales, H. Nakai, Raman spectra of carbon nanowalls grown by plasma-enhanced chemical vapor deposition, J. Appl. Phys. 97 (2005). https://doi.org/10.1063/1.1900297.
[40] K. Kobayashi, M. Tanimura, H. Nakai, A. Yoshimura, H. Yoshimura, K. Kojima, M. Tachibana, Nanographite domains in carbon nanowalls, in: J. Appl. Phys., American Institute of PhysicsAIP, 2007: p. 094306. https://doi.org/10.1063/1.2728781.
[41] S. Reich, C. Thomsen, Raman spectroscopy of graphite, (2004). https://doi.org/10.1098/rsta.2004.1454.
[42] A.C. Ferrari, D.M. Basko, Raman spectroscopy as a versatile tool for studying the properties of graphene, Nat. Nanotechnol. 8 (2013) 235–246. https://doi.org/10.1038/nnano.2013.46.
[43] S. Ghosh, K. Ganesan, S.R. Polaki, T.R. Ravindran, N.G. Krishna, M. Kamruddin, A.K. Tyagi, Evolution and defect analysis of vertical graphene nanosheets, (n.d.). https://doi.org/10.1002/jrs.4530.
[44] P. Venezuela, M. Lazzeri, F. Mauri, Theory of double-resonant Raman spectra in graphene: Intensity and line shape of defect-induced and two-phonon bands, Phys. Rev. B - Condens. Matter Mater. Phys. 84 (2011) 035433. https://doi.org/10.1103/PhysRevB.84.035433.
[45] M.A. Pimenta, G. Dresselhaus, M.S. Dresselhaus, L.G. Cançado, A. Jorio, R. Saito, Studying disorder in graphite-based systems by Raman spectroscopy, Phys. Chem. Chem. Phys. 9 (2007) 1276–1291. https://doi.org/10.1039/b613962k.
[46] B.B. Mandelbrot, B. B., The fractal geometry of nature /Revised and enlarged edition/, Whf. (1983).
[47] X. Shen, L. Li, W. Cui, Y. Feng, Improvement of fractal model for porosity and permeability in

porous materials, Int. J. Heat Mass Transf. 121 (2018) 1307–1315. https://doi.org/10.1016/j.ijheatmasstransfer.2018.01.084.

[48] W.H. Mulder, J.H. Sluyters, T. Pajkossy, L. Nyikos, Tafel current at fractal electrodes. Connection with admittance spectra, J. Electroanal. Chem. 285 (1990) 103–115. https://doi.org/10.1016/0022-0728(90)87113-X.

[49] L. Nyikos, T. Pajkossy, Fractal dimension and fractional power frequency-dependent impedance of blocking electrodes, Electrochim. Acta. 30 (1985) 1533–1540. https://doi.org/10.1016/0013-4686(85)80016-5.

[50] J.J. Dang, K.J. Chung, Y.S. Hwang, A simple spectroscopic method to determine the degree of dissociation in hydrogen plasmas with wide-range spectrometer, Rev. Sci. Instrum. 87 (2016). https://doi.org/10.1063/1.4948919.

[51] K. Teii, S. Shimada, M. Nakashima, A.T.H. Chuang, Synthesis and electrical characterization of n -type carbon nanowalls, J. Appl. Phys. 106 (2009). https://doi.org/10.1063/1.3238276.

[52] Z.H. Ni, T. Yu, Y.H. Lu, Y.Y. Wang, Y.P. Feng, Z.X. Shen, Uniaxial strain on graphene: Raman spectroscopy study and band-gap opening, ACS Nano. 2 (2008) 2301–2305. https://doi.org/10.1021/nn800459e.

[53] Z.H. Ni, H.M. Wang, Y. Ma, J. Kasim, Y.H. Wu, Z.X. Shen, Tunable stress and controlled thickness modification in graphene by annealing, ACS Nano. 2 (2008) 1033–1039. https://doi.org/10.1021/nn800031m.

[54] R. Silva, S.R.P. Silva, Raman spectroscopy of a-C, in: Prop. Amorph. Carbon, 2003: p. 49.

[55] and K. (Ken) O.* Dong Han Seo , Zhao Jun Han , Shailesh Kumar, Structure-Controlled, Vertical Graphene-Based, Binder-Free Electrodes from Plasma-Reformed Butter Enhance Supercapacitor Performance, (2013) 1316–1323. https://doi.org/10.1002/aenm.201300431.

[56] L.P. Biró, P. Lambin, Grain boundaries in graphene grown by chemical vapor deposition, New J. Phys. 15 (2013) 0–38. https://doi.org/10.1088/1367-2630/15/3/035024.

[57] J. Zhao, M. Shaygan, J. Eckert, M. Meyyappan, M.H. Rümmeli, A growth mechanism for free-standing vertical graphene, Nano Lett. 14 (2014) 3064–3071. https://doi.org/10.1021/nl501039c.

[58] S. Ghosh, K. Ganesan, S.R. Polaki, T. Mathews, S. Dhara, M. Kamruddin, A.K. Tyagi, Influence of substrate on nucleation and growth of vertical graphene nanosheets, Appl. Surf. Sci. 349 (2015) 576–581. https://doi.org/10.1016/j.apsusc.2015.05.038.

[59] Y. Ma, H. Jang, S.J. Kim, C. Pang, H. Chae, Copper-Assisted Direct Growth of Vertical Graphene Nanosheets on Glass Substrates by Low-Temperature Plasma-Enhanced Chemical Vapour Deposition Process, Nanoscale Res. Lett. 10 (2015). https://doi.org/10.1186/s11671-015-1019-8.

[60] L. Chong, H. Guo, Y. Zhang, Y. Hu, Y. Zhang, Raman study of strain relaxation from grain boundaries in epitaxial graphene grown by chemical vapor deposition on SiC, Nanomaterials. 9 (2019). https://doi.org/10.3390/nano9030372.